The International Journal of Advanced Manufacturing Technology (2023) 128:3427–3439
https://doi.org/10.1007/s00170-023-12165-8

ORIGINAL ARTICLE

Crystal plasticity–based finite element modeling and experimental study for high strain rate microscale laser shock clinching of copper foil

Yaxuan Hou[1] · Jianfeng Wang[1] · Zhong Ji[1] · Haiming Zhang[2] · Guoxin Lu[1] · Cunsheng Zhang[1]

Received: 20 December 2022 / Accepted: 13 August 2023 / Published online: 19 August 2023

Abstract
The microscale laser shock clinching (LSC) is a promising micro-forming technology that enables the deformation-based joining of ultra-thin sheets. In this research, a numerical crystal plasticity model of the LSC process at ultra-high strain rates is established to incorporate the actual grain size of the material and the anisotropic characteristics caused by different initial grain orientations. The simulations are in good agreement with the experiments, indicating that the crystal plasticity finite element method (CPFEM) can be used to study plastic deformation and predict the joint geometry during the LSC process. The results show that the joint can be divided into the material inflow zone, the interlock forming zone, and the material stacking zone. The material at the neck and underside experiences the most severe thinning and is prone to failure as being located at the junction, where the material flows in opposite directions on both sides. It is also found that the holes with different diameter-to-depth ratios in the perforated steel sheets greatly affect the neck thickness, a key mechanical strength factor in formed joints.

Keywords Micro-forming · Laser shock clinching · Crystal plasticity · Ultra-high strain rate

1 Introduction

Microscale metal forming is widely used to manufacture micro-parts due to its high efficiency and low cost [1]. At the micro/mesoscale level, the grain size is on the same order of magnitude as the thickness of the ultra-thin sheet. Studies have shown that there are significant differences in mechanical properties and deformation behavior between micro- and macro-forming because the grain's microstructural characteristics have a dominant influence on the deformation of the metallic material. Chan et al. [2] investigated the micro-compression of pure copper and discovered that inhomogeneous deformation and scattering of experimental data occur when the specimen consists of only a few grains. Qu et al. [3] found that grain inhomogeneity plays an important role in micro-rolling in terms of the rolling force and springback of the workpiece. Shimizu et al. [4] performed micro-deep drawing tests of ultra-thin rolled metal foils and confirmed that surface roughening associated with crystal grain and equivalent strain is responsible for the unstable deformation. Wang et al. [5] demonstrated that the material failure in blanking process of ultra-thin sheets exhibits deterministic size effects. Although the deformation processes mentioned above are conducted at quasi-static or low strain rates, a more comprehensive study of microscale metal forming that takes into account the microstructural characteristics and the anisotropic features of the material is always essential.

Laser shock clinching (LSC), a special laser shock–forming technology, provides a viable solution for plastic deformation-based joining of materials in dynamic or high strain rates metal-forming processes [6]. This technology has great potential applications, especially in the micro-manufacturing industry. The LSC process relies on the deformation forces arising from the violently exploded plasma induced by the interaction between the pulsed laser and the absorptive layer. The resulting shock pressure can exceed 1.0 GPa, and the strain rate of the

✉ Zhong Ji
jizhong@sdu.edu.cn

[1] School of Materials Science and Engineering, Shandong University, 17923 Jingshi Road, Jinan 250061, Shandong, China

[2] Institute of Forming Technology & Equipment, School of Materials Science and Engineering, Shanghai Jiao Tong University, Shanghai 200030, China

sheet typically exceeds 10^6/s [7]. The LSC technology was initially invented by Ji et al. [8] and has been investigated by many scholars in recent years. Veenaas et al. [6, 7] deformed aluminum foils by TEA-CO_2 laser and successfully joined them with perforated steel sheets, and extended this technique to the joining of Al/glass [9] and Al/plastic [10]. Wang et al. [11, 12] investigated the LSC process of similar and dissimilar foils and implemented the Johnson-Cook (J-C) constitutive model in the finite element method (FEM). Zheng et al. [13] explored the joining behavior and the influence of process parameters on the joints of Cu/Fe. Hou et al. [14] proposed an improved LSC process namely flat-hole clinching to eliminate geometric protrusions in visible or functional regions. Although the effects of technical parameters such as laser power and die geometry on the LSC process have been extensively studied by experiments and conventional FEM, only a few works [15] have considered the microstructure and anisotropic characteristics of the material in experiments. Moreover, the conventional FEM commonly used has an inherent weakness in the response of the material microstructure.

The crystal plasticity finite element method (CPFEM) is an effective tool for describing the microstructural and anisotropic characteristics of materials, which is considered to be the key to improving the accuracy of microforming simulation. Li et al. [16] studied the compression process of cylinder aluminum by combining crystal plasticity theory and macroscopic FEM, and the results showed that the microscopic features of the material such as crystal orientation, misorientation, and grain boundary have significant influences on the inhomogeneous deformation. Zhang et al. [17] adopted a crystal plasticity model to simulate the micro-deep drawing process and demonstrated that significant differences in plastic deformation between grains contribute to the poor forming quality of the drawing cups. Barrett et al. [18] also reached a similar conclusion through experimental validation and a polycrystalline homogenization model embedded in implicit finite elements. Other processes like micro-rolling [3], micro-upsetting [19], helical extrusion [20], and microscale tensile tests [21] have also been explored based on the crystal plasticity model. And the micro-grinding process has also been investigated through a Taylor factor model [22]. However, these deformation processes are all performed at low strain rates, where the constitutive models and the corresponding computational methods are not suitable for high strain rate processes. Wang et al. [23] established disk-shaped polycrystalline aggregates with different initial grain sizes to simulate a laser shock-bulging process and compared it with our previous work [15]. It is worth noting that this bulging deformation is very simple and small, with a maximum dome height of only 0.6 mm. As far as we know, previous studies have not implemented the CPFEM to investigate complex deformations with high or ultra-high strain rates like the microscale LSC process.

In this study, a numerical model of crystal plasticity for the microscale LSC process is developed considering the microstructural characteristics and anisotropic features of the material. The established CPFEM model has the ability to capture the individual or specific grain orientation effect. By incorporating the actual grain size and initial grain orientations, it can accurately model the anisotropic behavior of materials and predict their mechanical response, which provides valuable insights into the deformation behavior of materials at the microscale. The constitutive equation integrates the dislocation motion dominated by the thermally-activated process and the drag-dominated process. The deformation behavior is investigated by CPFEM simulations and experiments, which not only improves the understanding of microscale LSC process but also promotes the application of CPFEM in ultra-high strain rate deformation.

2 Experiment and simulation preparation

2.1 Experimental setup

The microscale LSC process is a versatile technology for joining ductile and brittle sheets, regardless of whether they are similar or dissimilar in material type and thickness. Figure 1 presents a schematic of the LSC process. The copper foil undergoes plastic deformation under the pressure of shock waves generated by the laser with high power density and short pulses, which eventually creates a geometrical interlock between the copper foil and the perforated steel sheet. Applying an ablative layer (black paint) between the confinement layer (quartz glass) and the copper foil not only protects the metal surface, but also enhances the transfer of laser energy to the material, thereby significantly increasing the intensity of shock waves.

The 2-cm square specimens of copper foil and steel sheet with thicknesses H_1 and H_2 are joined to obtain a geometric interlocking structure under the action of the Nd: YAG laser system. The material and laser system parameters are given in Table 1. Prior to the LSC process, a heat treatment is applied to the copper foil to eliminate the effect of rolling direction. The micrographs of the annealed copper foil at 400 °C for 1 h in a vacuum furnace are shown in Fig. 2. As can be seen from the two locations presented in Fig. 2, the grain distribution is generally uniform and the initial average grain size is of the identical order of magnitude as the thickness of the copper foil. Only very few grains can be observed in the direction of the material thickness.

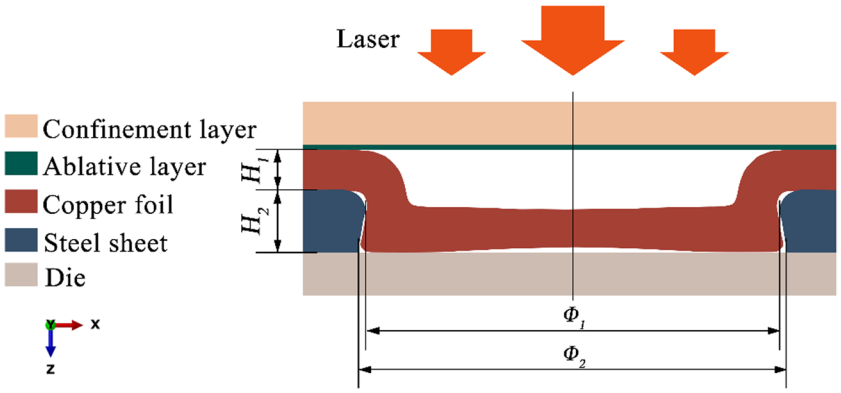

Fig. 1 Schematic diagram of the LSC process

Table 1 Specific parameters of the material and the laser

Parameter	Value
Φ_1 (mm)	0.80
Φ_2 (mm)	0.84
H_1 (μm)	20
H_2 (μm)	100
The laser pulse width τ (ns)	12.00
The laser spot diameter d (mm)	6.00
The laser energy E(J)	1.60 + 3.00 [14]

2.2 Pressure distribution model

The material undergoes plastic deformation under the pressure of the laser-induced shock waves. The equation for the temporal and spatial distribution of the pressure is given by [24, 25]

$$P(r,t) = 10^{-9}\sqrt{\alpha/(2\alpha+3)\cdot Z\cdot\left(4E/\pi d^2\tau\right)}\cdot N(t)\cdot\exp\left(-2r^2/d^2\right) \quad (1)$$

where $P(r,t)$ is the pressure value at the radial distance r from the center of the laser spot at the moment t. α is the coefficient of energy transformation and represents the portion of internal energy devoted to thermal energy (generally taken as 0.10). Z is defined as $Z=2Z_1Z_2/(Z_1+Z_2)$, related to the impedance of the copper foil $Z_1= 3.83\times10^{10}$ g/(m^2 s) and the impedance of the quartz glass $Z_2= 1.31\times10^{10}$ g/(m^2 s). Thus, here $Z = 1.95\times10^{10}$ g/(m^2 s) [15, 23, 26]. $4E/\pi d^2\tau$ is considered as the laser power density and E, d, and τ are the laser energy, the laser spot diameter, and the laser pulse width, respectively. $N(t)=\begin{cases} t/\tau\ (0\le t\le\tau) \\ (3\tau-t)/2\tau\ (\tau<t\le3\tau)\end{cases}$, which simplifies the curve of pressure versus time to a triangle for a single laser shock. The non-uniformity of the

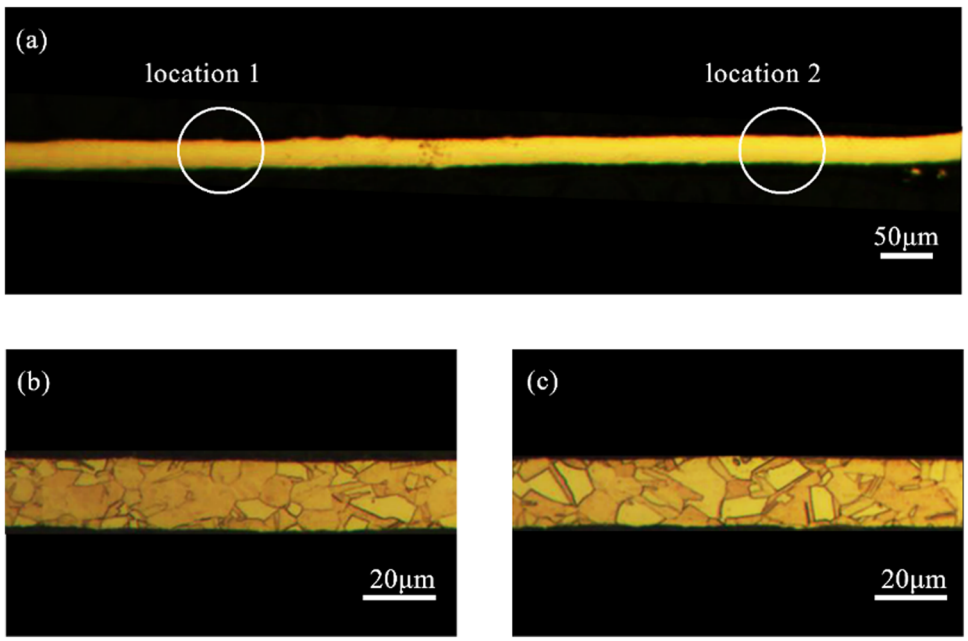

Fig. 2 Macro/microstructure along the thickness of the copper foil. **a** Macro view. **b** Location 1. **c** Location 2

laser shock wave pressure in space is depicted by a Gaussian distribution [27].

2.3 Constitutive model of crystal plasticity

Based on the continuum mechanics and crystal plasticity theory, the deformation gradient can be expressed as $F = \partial x/\partial X$, which is decomposed into the multiplication of the elastic gradient and the plastic gradient, rewritten as $F = F^e F^P$, where X and x are the coordinates in the initial and current configurations, respectively. F^e and F^P are the elastic and plastic gradients, respectively. Therefore, the process of crystal plastic deformation can be considered as the lattice undergoes inelastic shear deformation to the intermediate configuration and further occurs rotational and elastic deformation to the current configuration, as shown in Fig. 3. The Schmid resolved tensor S_0^α is expressed as $S_0^\alpha = m_0^\alpha \otimes n_0^\alpha$, where α refers to the slip system. m_0^α denotes the slip direction. n_0^α denotes the slip plane normal.

The Green-Naghdi material co-rotation frame, a moving coordinate system that rotates with the material, is used in ABAQUS/Explicit and many other explicit solvers to handle large-scale deformation and rotation problems while achieving incremental objectivity. The stress update scheme in this paper is based on the unrotated intermediate configuration using the stress and strain tensor of the material without any additional transformations [17]. The initial orientation of aggregated grains in a polycrystalline material is defined by the Bunge's Euler angle, which is commonly used to describe the crystallographic texture (or preferred orientation) and provide a mathematical description of the orientation of individual crystals in polycrystalline materials. It is possible to obtain any orientation by combining three elemental rotations, starting from a standard orientation that is already known. Therefore, this CPFEM model has the ability to capture the individual or specific grain orientation effect. The rotation matrix Q can be expressed as

$$Q = \begin{bmatrix} \cos\varphi_1\cos\varphi_2 - \sin\varphi_1\sin\varphi_2\cos\Phi & \sin\varphi_1\cos\varphi_2 + \cos\varphi_1\sin\varphi_2\cos\Phi & \sin\varphi_2\sin\Phi \\ -\cos\varphi_1\sin\varphi_2 - \sin\varphi_1\cos\varphi_2\cos\Phi & -\sin\varphi_1\sin\varphi_2 + \cos\varphi_1\cos\varphi_2\cos\Phi & \cos\varphi_2\sin\Phi \\ \sin\varphi_1\sin\Phi & -\cos\varphi_1\sin\Phi & \cos\Phi \end{bmatrix} \tag{2}$$

The velocity gradient L is defined as $L = \dot{F} \bullet F^{-1}$, which can be decomposed as $L = D + W$, where D and W are the stretching and spin tensors, respectively, which is further decomposed into the elastic and plastic parts as follows [28]:

$$D^e = \frac{L^e + L^{eT}}{2}, W^e = \frac{L^e - L^{eT}}{2} \tag{3}$$

$$D^P = \frac{L^P + L^{PT}}{2} = \sum_{\alpha=1}^{N} P^\alpha \bullet \dot{\gamma}^\alpha, W^P = \frac{L^P - L^{PT}}{2} = \sum_{\alpha=1}^{N} W^\alpha \bullet \dot{\gamma}^\alpha \tag{4}$$

where $\dot{\gamma}^\alpha$ is the slip rate of the αth slip system, and

$$P^\alpha = \frac{m_0^\alpha \otimes n_0^\alpha + n_0^\alpha \otimes m_0^\alpha}{2}, W^\alpha = \frac{m_0^\alpha \otimes n_0^\alpha - n_0^\alpha \otimes m_0^\alpha}{2} \tag{5}$$

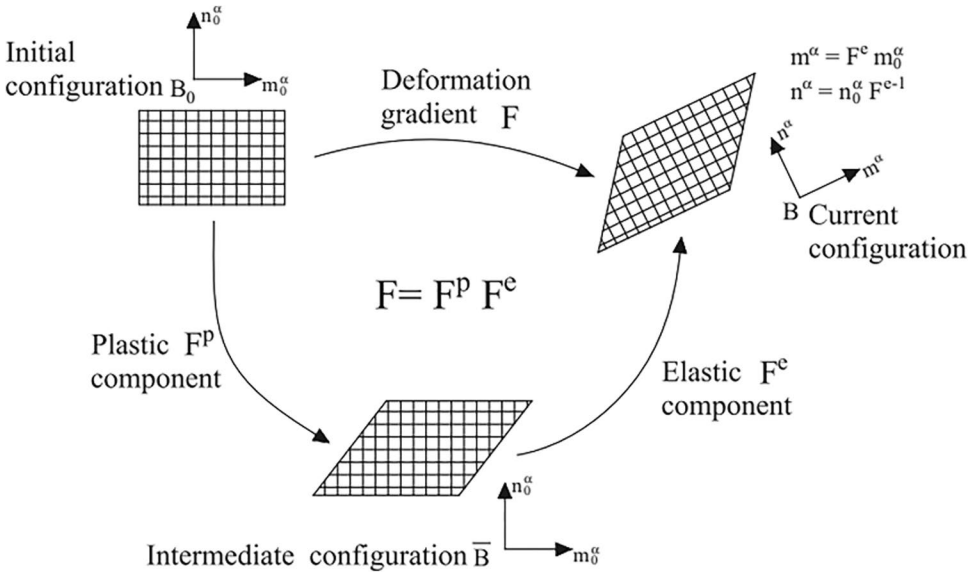

Fig. 3 Schematic of deformation gradient [33]

Under the condition of realizing incremental objectivity, the constitutive model is established in the intermediate configuration as follows:

$$\Delta\sigma = C^e \Delta\varepsilon - \sum_{\alpha} R^{\alpha} \Delta\gamma^{\alpha} \tag{6}$$

$$R^{\alpha} = C^e P^{\alpha} + W^{\alpha}\sigma - \sigma W^{\alpha} \tag{7}$$

where C^e is the elastic tensor and is determined by three independent constants (C_{11}, C_{12}, C_{44}). A linear interpolation and a Taylor expansion are employed to obtain [29]

$$\Delta\gamma^{\alpha} = \Delta t\left(\dot{\gamma}_t^{\alpha} + \theta \bullet \frac{\partial \dot{\gamma}_t^{\alpha}}{\partial \tau^{\alpha}} \bullet \Delta\tau^{\alpha} + \theta \bullet \frac{\partial \dot{\gamma}_t^{\alpha}}{\partial g^{\alpha}} \Delta g^{\alpha}\right) \tag{8}$$

where the increment of the resolved shear stress $\Delta\tau^{\alpha}$ can be calculated from

$$\Delta\tau^{\alpha} = P^{\alpha}\Delta\sigma \tag{9}$$

The evolution of the slip system resistance is given by [30]

$$\Delta g^{\alpha} = \sum_{\beta} h^{\alpha\beta} \Delta\gamma^{\beta} \tag{10}$$

$$h^{\alpha\beta} = h_0\left[q + (1-q)\delta^{\alpha\beta}\right]\left|1 - \frac{g^{\beta}}{g^{s}}\right|^{a} \tag{11}$$

Table 2 Parameters of crystal plasticity model [17, 23, 30]

Parameter	Value
$\dot{\gamma}_0^{\alpha}(s^{-1})$	1.00×10^{7}
E_0(J)	1.00×10^{-18}
K(J·K^{-1})	1.38×10^{-23}
T(K)	300.00
g_0^{α}(MPa)	16.00
g^{s}(MPa)	148.00
h_0(MPa)	180.00
C_{11}(GPa)	186.00
C_{12}(GPa)	93.00
C_{44}(GPa)	46.50
b(nm)	0.26
B_0	3.84
b_1	12.79
b_2	-5.00×10^{-6}
m_1	0.33
m_2	1.66
θ	0.50
a	2.25

where $h^{\alpha\beta}$ is the hardening modulus, describing both self-hardening and latent-hardening of the slip systems. h_0 is the self-hardening parameter. q is the latent-hardening parameter and is taken as 1.0 and 1.4 for coplanar and non-coplanar slip systems, respectively. g^{s} is the saturation stress and a is a constant.

The plastic slip-rate $\dot{\gamma}_t^{\alpha}$ is developed from the following unified flow rule [23, 31, 32]

$$\dot{\gamma}_t^{\alpha} = \dot{\gamma}_0^{\alpha} \cdot \mathrm{sgn}(\tau^{\alpha})\left\{(1-\epsilon)\cdot\exp\left[-\frac{E_0}{KT}\left\langle 1 - \left\langle \frac{|\tau^{\alpha}| - g^{\alpha}}{g_0^{\alpha}}\right\rangle^{m_1}\right\rangle^{m_2}\right] + \epsilon \cdot \frac{\langle|\tau^{\alpha}| - g^{\alpha}\rangle \cdot b}{B}\right\} \tag{12}$$

where $\langle\ \rangle$ represents $\langle x\rangle = \begin{cases} x(x \geq 0) \\ 0(x < 0) \end{cases}$. E_0, K, and T are the thermal barrier energy, Boltzmann constant, and temperature, respectively. $g_0^{\alpha}$is the initial slip system resistance and b is the magnitude of the Burgers vector. B is the viscous drag coefficient, related to the material and the strain rate $\dot{\varepsilon}$, whose exact value is defined by the fitted equation $B = B_0 + b_1 \cdot \exp\left(b_2 \cdot \dot{\varepsilon}\right)$. The constitutive model integrally takes into account the dislocation motion dominated by the thermally-activated process or the drag-dominated process, which is useful for simulating the plastic deformation of metals at high strain rates. Eq. (12) is divided into two parts according to the relative relationship between the values of $|\tau^{\alpha}| - g^{\alpha}$ and g_0^{α}. When $\epsilon = 0$, the dislocation motion in metals is governed by the thermally-activated process and the formula degenerates into a power law model. When $\epsilon = 1$, it is dominated by the drag-dominated process and the formula degenerates into a linear function. Substituting Eqs. (8)–(11) into Eq. (12) yields $\Delta\gamma^{\alpha}$. Table 2 indicates the parameters of the copper foil used for the CPFEM model.

2.4 J-C constitutive model

The J-C constitutive model is conventionally used to describe the high strain rate deformation processes in metallic materials [11]. Previous studies of the microscale LSC process have widely adopted the J-C model for macroscopic modeling. The crystal plasticity model developed in this study was compared with the J-C model, in which specific material parameters were taken from the literature [14]. The yield stress equation for von-Mises in the J-C model is

$$\sigma_{\gamma} = \left(A + B\overline{\varepsilon}^{n}\right)\left(1 + C\ ln\ \overline{\varepsilon}^{*}\right)\left(1 - \left[(T - T_0)/(T_m - T_0)\right]^{m}\right) \tag{13}$$

where σ_γ, $\overline{\varepsilon}$, $\overline{\varepsilon}^*$ are the equivalent stress, equivalent plastic strain, and strain rate, respectively. T_0 and T_m are the room temperature and the melting point of the material. A, B, C, m, and n are material constants.

3 Implementation of crystal plasticity

3.1 Polycrystalline model selection

The Taylor-type model in the mean-field crystal plasticity was adopted as the polycrystalline model, which can provide an ideal prediction of anisotropy results [33]. The Taylor-type model assumes that the strain in a single crystal is identical to the macroscopic strain of the polycrystalline. The macroscopic stress of the polycrystalline material can be simplified as the volume average of the co-rotational stress at the material point, under the condition that all grains have the same volume.

Uniaxial compression simulations were performed on a single cube ($1 \times 1 \times 1$ mm) to validate and compare polycrystalline models in the CPFEM. The constitutive model of crystal plasticity was numerically implemented in the finite element code ABAQUS/Explicit via a user-defined material subroutine (VUMAT). Four combinations of polycrystalline models were determined based on the equal total number of grains (also grain size) and the same mesh type (C3D8R). The "number of elements × number of grains" was employed to represent different polycrystalline models, namely 1 element × 512 grains, 8 elements × 64 grains, 64 elements × 8 grains, and 512 elements × 1 grain. The initial orientations of the grains used in the different polycrystalline models were taken from the same file, while the 512 grains had random and diverse initial orientations. The bottom surface of the model was completely constrained in the vertical direction, while the top surface was subjected to a displacement of 0.4 mm.

Figure 4 presents the simulated true strain distributions of four polycrystalline models comprising a total of 512 grains at the same deformation time. The diversity of strain values in the cubic increases as the number of elements increases, indicating an increment in the degree of deformation inhomogeneity. This is due to the limitation of inhomogeneity within each element by the simplicity of the finite element displacement function [34]. Therefore, with the same total number of grains, the more elements, the fewer grains each element contains, leading to more significant deformation inhomogeneity. The unique CPFEM model, "512 elements × 1 grain" shown in Fig. 4d, uses one element to represent one grain. This model satisfies both strain coordination and stress balance conditions, and is simple, practical, and efficient for engineering applications [35], with the ability to capture individual or specific grain deformation.

Figure 5 presents a comparison of the resultant displacements obtained from the CPFEM (512 elements × 1 grain) and the J-C model (512 elements). As shown in Fig. 5b, the displacements of the CPFEM model and the J-C model along

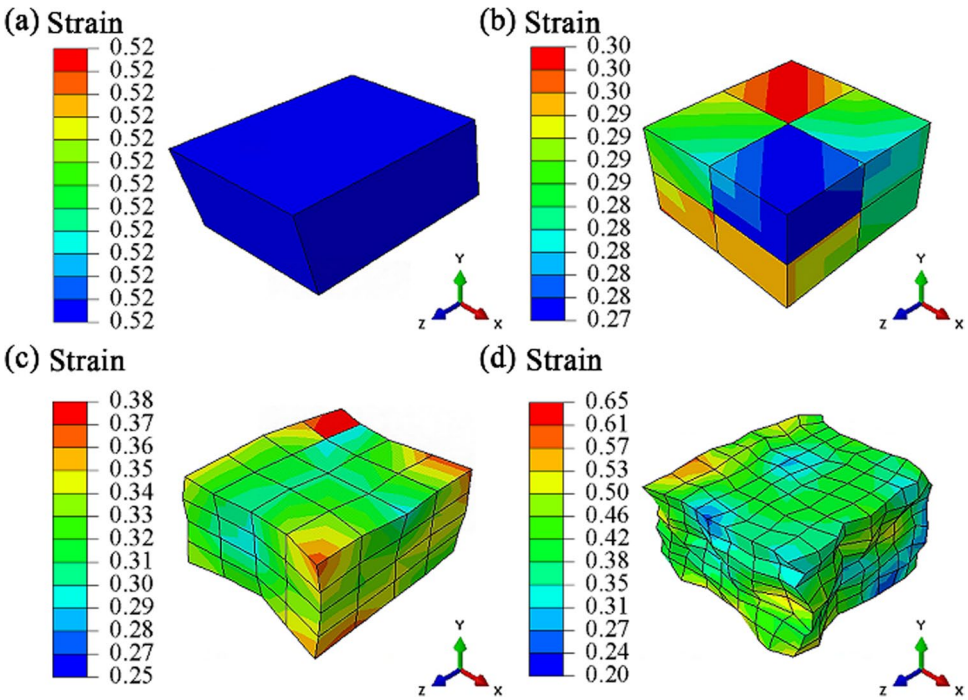

Fig. 4 True strains for four polycrystalline models. **a** 1 element × 512 grains. **b** 8 elements × 64 grains. **c** 64 elements × 8 grains. **d** 512 elements × 1 grain

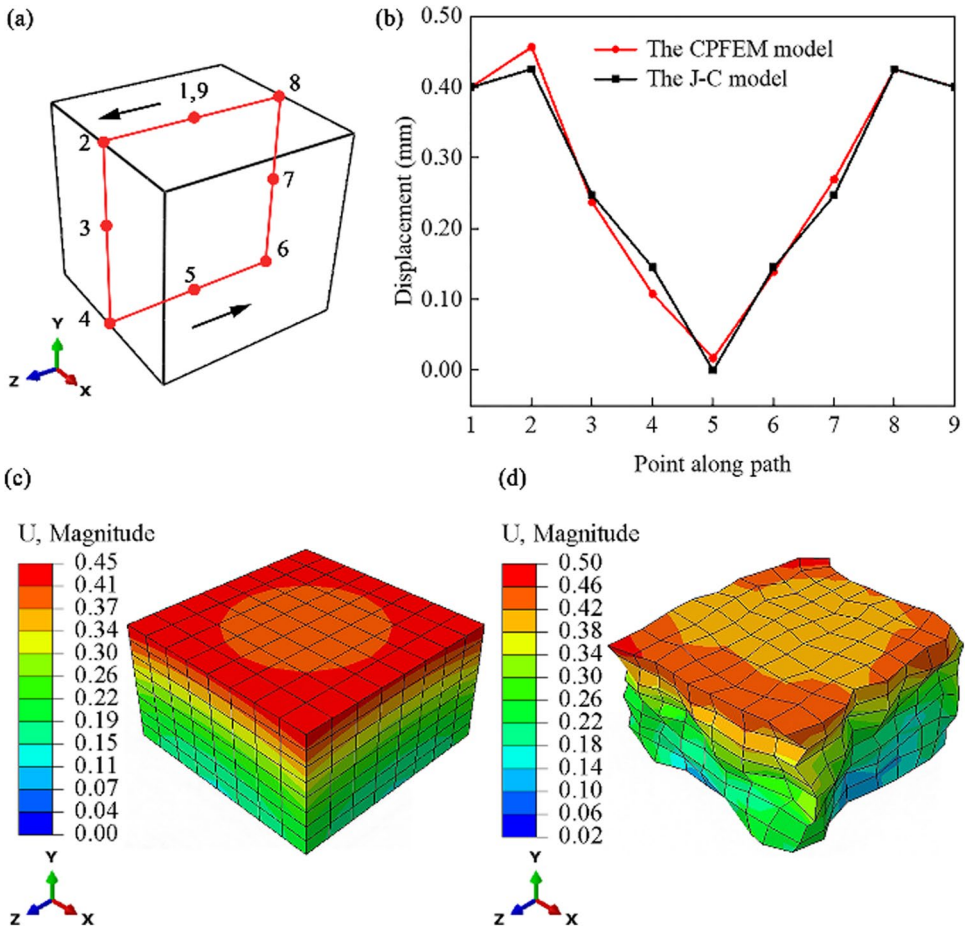

Fig. 5 Displacement distributions. **a** Diagram of the path. **b** Comparison along the path. **c** J-C model. **d** CPFEM model

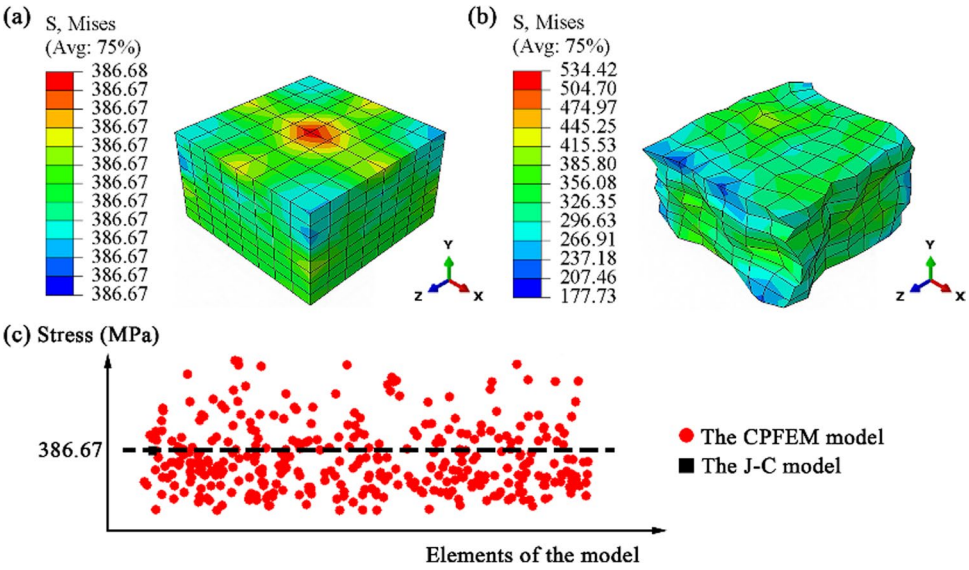

Fig. 6 Comparison of stresses obtained from CPFEM model and J-C model. **a** J-C model. **b** CPFEM model. **c** Comparison of stress distributions

the path shown in Fig. 5a are in good agreement. The displacement distribution of the J-C model presented in Fig. 5c is highly uniform and symmetric about the center in the Z-direction, while the CPFEM model presented in Fig. 5d is non-uniform and asymmetric. It shows that the CPFEM model can obtain reasonable displacement distributions and exhibit the deformation inhomogeneity of the material due to the differences in microscopic grain orientations.

Figure 6 compares the stresses obtained from the CPFEM model and the J-C model. The stress distribution in the J-C model gives very consistent results, concentrated at 386.67 MPa, as shown in Fig. 6a. For the CPFEM mode, it has a wide range of stress distribution from 177.73 MPa to 534.42 MPa, as shown in Fig. 6b. The Mises stresses for each element in the CPFEM model are extracted and displayed as red dots in Fig. 6c. It is noteworthy that the CPFEM model tends to concentrate the stress values around 386.67 MPa. The polycrystal can be approximated as an aggregate of a large number of single elements when the number of elements is large enough. Therefore, it is feasible to select the unique CPFEM model as the polycrystalline model for crystal plasticity simulations of the LSC process. The CPFEM models mentioned later all refer to this type of polycrystalline model.

3.2 Crystal plasticity model for the LSC process

The microscale LSC process for joining a 20 μm copper foil and a 100 μm perforated steel sheet was simulated by the CPFEM model developed with the VUMAT subroutine embedded in ABAQUS/Explicit. Two laser shocks were adopted and the temporal and spatial distributions of the laser pressure were obtained from Eq. (1), with specific parameters taken from Table 1. The calculated peak pressures for the two shocks were 1.70 GPa and 2.24 GPa. The relevant parameters for the crystal plasticity model were taken from Table 2. The CPFEM model was adopted as the polycrystalline model, where one element represented one grain. A mesh size of 0.01 mm was determined considering the actual grain size in Fig. 2 and the effect of element size on the simulation accuracy. The copper foil model contained a total of 20,000 elements, each assigned a random Euler angle, which refers to a polycrystalline aggregate with differently oriented grains.

In the LSC process, the material deforms at ultra-high strain rates under the action of high power and short-pulsed lasers. The previously validated uniaxial compression simulations were performed at a high strain rate, so there is still a need to further validate the applicability of the developed crystal plasticity model at ultra-high strain rates. Figure 7 shows a comparison of simulations and experiments of the joint after one single laser shock. The CPFEM model accurately predicts the material thickness at key locations, demonstrating good agreement with experiments, with a maximum dimensional error of 4.26%. Therefore, the numerical model based on crystal plasticity can simulate the complex deformation behavior of the material at ultra-high strain rates, and it is feasible to simulate the LSC process.

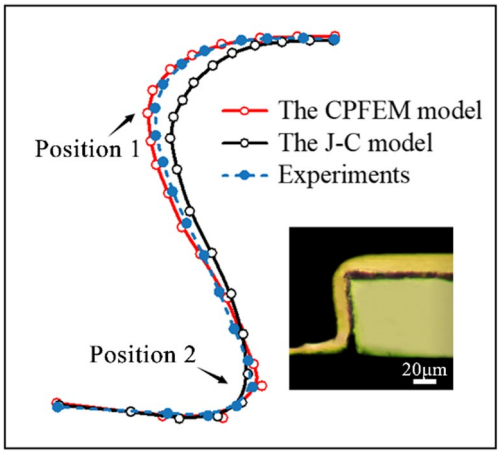

Fig. 8 Comparison of the upper surface profile on the right side of the joint

After two laser shocks, the copper foil was indented into the cavity and formed a geometric interlock. Figure 8 presents the upper surface profile curves on the right side of the joints obtained from simulations and experiments. At Position 1, the joint profile obtained from the CPFEM model agrees well with the experimental results, while there is a discrepancy between the joint profile obtained from the J-C model and experiments. At Position 2, the joints obtained from the simulations, both the CPFEM model and the J-C model, show little deviation from experiments. In general, the CPFEM model provides a viable means of predicting the joint profile, which improves the accuracy of the simulation.

4 Deformation behavior of the LSC process

4.1 Deformation process

The deformation process of the copper foil during the microscale LSC process was explored based on the

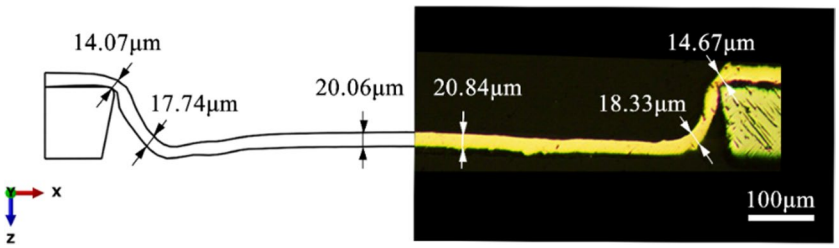

Fig. 7 Comparison of simulated (left) and experimental (right) joints after one laser shock

established crystal plasticity model, as shown in Fig. 9. In Stage 1, from the beginning to the moment t = 6.25e−7 s as shown in Fig. 9a, the copper foil flowed into the cavity of the steel sheet under the action of the first laser pulse and the material was mainly deformed in the Z-direction. The deformation mode shifted to Stage 2 when the bottom of the foil contacted the die, resulting in a state as presented in Fig. 9b, where the central material underwent significant deformation in the opposite Z-direction through the propagation of the laser shock waves. In

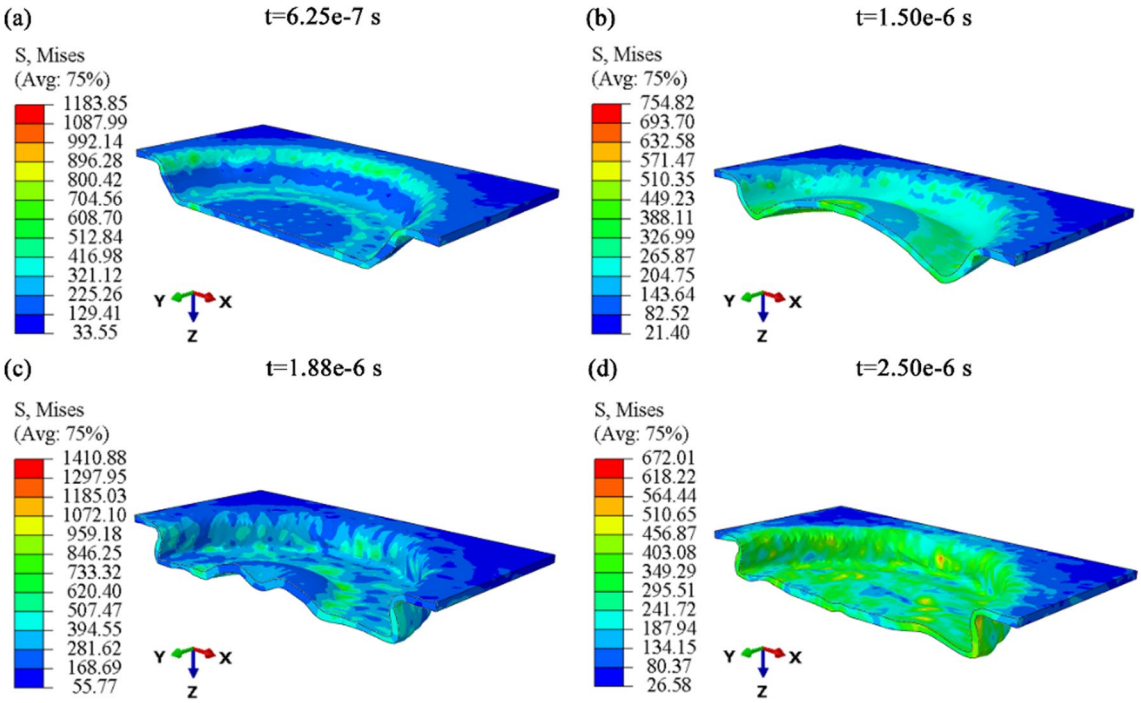

Fig. 9 Deformation process during LSC

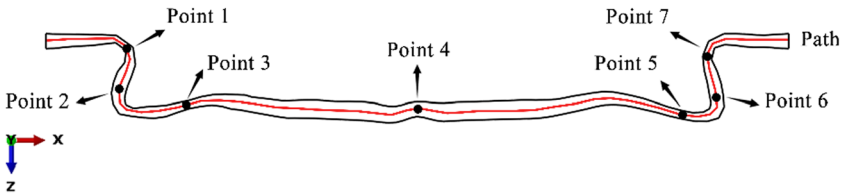

Fig. 10 Cross-section profile of the simulated joint and the observed path and key points

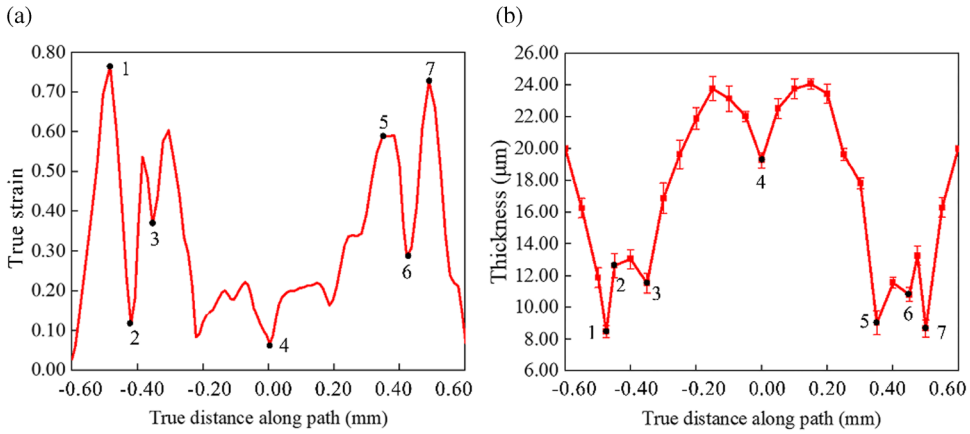

Fig. 11 True strain and thickness distribution along the path

Stage 3, the central material started to move downwards in response to the second laser shock, maintaining a similar "M" shape as displayed in Fig. 9c. It is during this stage that the geometric interlocking of the joint gradually develops. The microscale LSC process is completed after the formation of the undercut structure of the joint, as illustrated in Fig. 9d.

4.2 Material flow

To further investigate the material flow during the microscale LSC process, the deformation behavior along the path marked with a red curve and the key points highlighted in Fig. 10 was further observed. Figure 11a exhibits the true strain distribution along the path. It is approximately symmetrical about the specimen center in the X-direction, which is consistent with the assumption that the metal is regarded as a homogeneous unit at the macroscopic level. The non-absolute symmetry is caused by the different grain orientations, which describe the heterogeneous material properties and microscopic anisotropy. Figure 11b indicates the thickness distribution of the formed joint. It can be seen that the higher the strain value, the thinner the material. The most severe material thinning occurs at the neck (Points 1, 7) and the underside (Points 3, 5) of the joint, while the material accumulation appears at the bottom near the center. It is noteworthy that the thickness of the foil at the center of the specimen keeps almost unchanged.

The time-displacement curves of the key points were presented in Fig. 12. Overall, the material flow mainly occurs in the X and Z directions, with little material flow in the Y

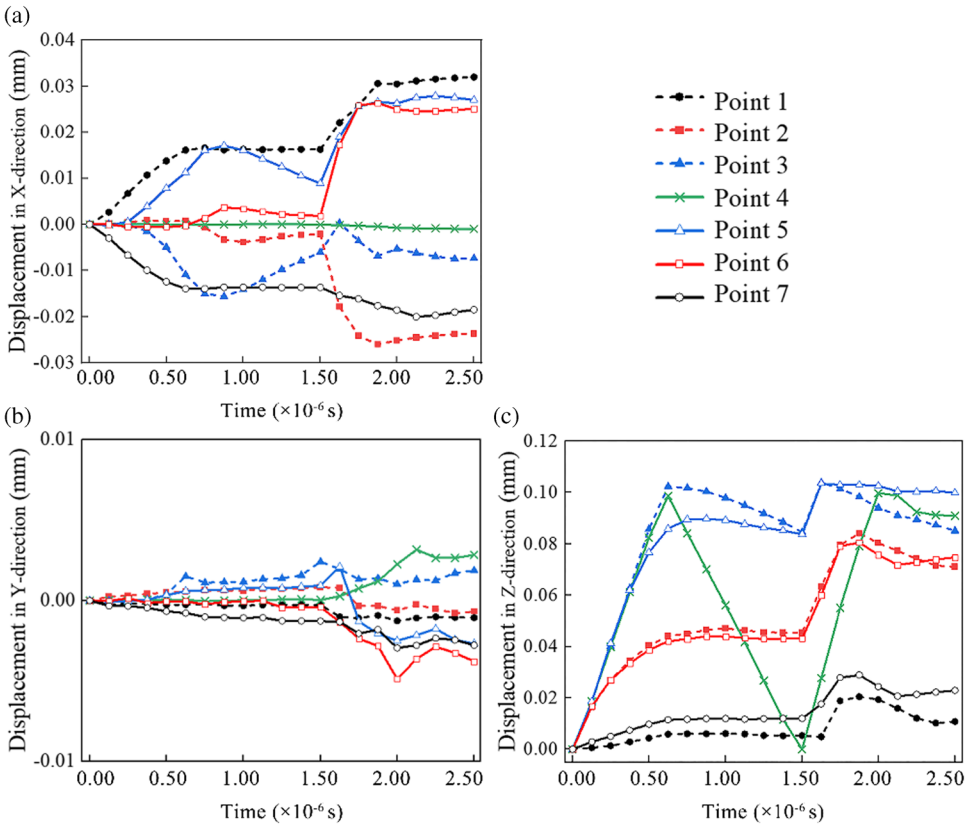

Fig. 12 Time-displacement curves for key points. **a** X-direction. **b** Y-direction. **c** Z-direction

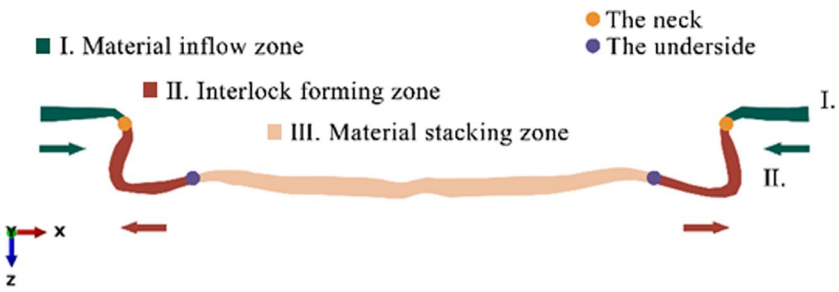

Fig. 13 Three zones of formed joints based on the material flow

direction. As can be seen from Fig. 12a, the points located at corresponding positions on either side of the laser spot center have X-directional displacement values of equal magnitude and opposite directions. The displacement of Point 4 is essentially zero. This indicates that the material flow in the X-direction is symmetrical about the center, and the central material experiences no obvious X-directional flow during the entire deformation process. After t = 1.50e−6 s, the displacements of Points 2 and 6 exhibit a surge in the X-direction, indicating that the formation of the interlocking structure relies heavily on the material flow in the X-direction near the undercut of the joint during Stage 3 of the deformation process.

Based on the above analysis of the deformation behavior, the deformed joint can be classified into three zones as shown in Fig. 13: (I) material inflow zone, (II) interlock forming zone, and (III) material stacking zone. In zones I and III, the material flows towards the center of the joint, where it converges and flows into the cavity of the perforated sheet. However, in zone II, the material flows away from the center of the joint, where it fits into the perforated sheet to form the interlocking structure. The neck and underside locations, marked with dots in Fig. 13, experience the most material thinning and are most prone to material failure. It is attributed to the fact that these locations are at junctions where the material flows in opposite directions on either side.

4.3 Effect of diameter-to-depth ratio on joints

The CPFEM has the advantage of predicting the joint profile and effectively avoids the negative effects of experimental errors when the workpiece is very small. The small holes with different diameter-to-depth ratios (λ) in the perforated sheets were molded and their effects on the microscale LSC process were investigated with CPFEM. The thickness of the perforated sheet was kept at 100 μm and the taper of the holes was maintained at 10°. The diameter-to-depth ratios (λ) of the holes and their corresponding upper diameters are listed in Table 3.

Table 3 Different diameter-to-depth ratios of holes in perforated sheets

Φ_1(mm)	Diameter-to-depth ratio λ
0.40	4.00
0.45	4.50
0.50	5.00
0.55	5.50
0.60	6.00
0.65	6.50
0.70	7.00
0.75	7.50
0.80	8.00

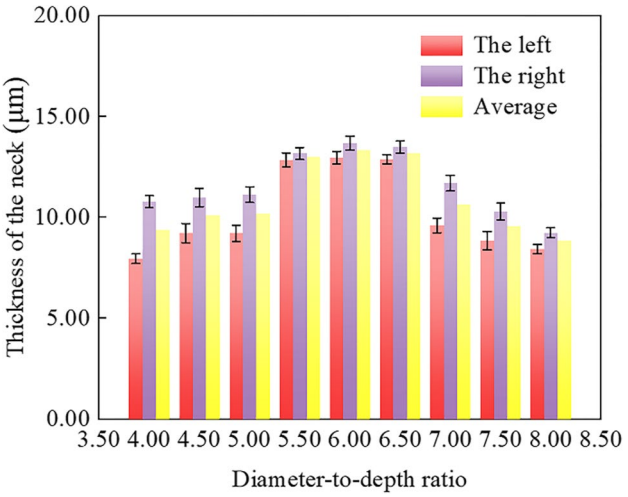

Fig. 14 Neck thickness of joints formed with different diameter-to-depth ratios

It is clear from previous studies that the strength of a successfully interlocked joint depends on the neck thickness of the joint. Figure 14 exhibits the left, right, and average neck thicknesses of the joints with λ ranging from 4.00 to 8.00. These cases have an equal number of grains with the same initial grain orientations and orientational distribution to ensure comparability. The variation between grain orientations in each case causes the material to exhibit anisotropic properties, which results in different neck thicknesses on the left and right sides of the same joint, always showing the right side higher than the left.

For the thickness combination of 20 μm copper foil and 100 μm steel sheet, the neck thickness shows a trend of first increasing and then decreasing when λ ranges from 4.00 to 8.00. It implies that the diameter-to-depth ratio plays a crucial role in the material flow and joint formation. From the above discussion, it can be concluded that joints with a λ of 8.00 experience material thinning to fill the cavity and form the final shape due to the larger hole. Similar patterns are observed for λ values from 7.00 to 8.00. In contrast, the hole is smaller and the material is squeezed into the cavity to form a joint when λ ranges from 4.00 to 5.00. In both cases, smaller neck thicknesses are obtained. Joints with λ values from 5.50 to 6.50 present an intermediate state between the two formation mechanisms mentioned above, and have relatively large neck thicknesses as a result of a lower degree of thinning and squeezing. There is little difference in neck thickness in this intermediate state as the perforated sheets have close-hole diameters. Therefore, the maximum neck thickness and better mechanical properties of the joint are achieved at a λ of 6.00 for the combination of 20 μm copper foil and 100 μm steel sheet used in this study.

5 Conclusion

In this paper, a CPFEM model for the microscale LSC process was established and implemented in ABAQUS/Explicit with the VUMAT subroutine. The numerical simulations are in good agreement with the experiments and have advantages in simulating the deformation behavior and microstructural characteristics of the material. The main conclusions are as follows:

(1) A numerical crystal plasticity model for the microscale LSC process at ultra-high strain rates is developed, which is in good agreement with the experimental results and provides a better representation of the joint profile than the macroscopic model.
(2) The formation of the interlocking structure is mainly attributed to the material flow in the X-direction at the undercut. The joint is divided into three zones according to the material flow, namely material inflow zone, interlock forming zone, and material stacking zone.
(3) The diameter-to-depth ratio of the hole in the perforated sheet plays a vital role in the material flow and joint formation. For the material combinations studied in this paper, the thickest neck of the joint is obtained for a diameter-to-depth ratio of 6.00.

Author contributions Yaxuan Hou: conceptualization, methodology, software, writing—original draft preparation; Jianfeng Wang: visualization; Zhong Ji: supervision, validation, writing—reviewing and editing; Haiming Zhang: supervision; Guoxin Lu: data curation; Cunsheng Zhang: writing—reviewing

Funding This work is supported by the National Natural Science Foundation of China (Nos. 52075298, 52171073), the Science Fund for Distinguished Young Scholars of Shandong Province (JQ201810), and the Fund of the State Key Laboratory of Solidification Processing in NPU (No. SKLSP202014).

Data availability All data generated or analyzed during this study are included in this published article.

Code availability Not applicable.

Declarations

Ethics approval The authors declare that this study is original and has not been published elsewhere.

Consent to participate The authors declare that they consent to participate in this paper.

Consent for publication This manuscript is approved by all authors for publication.

Competing interests The authors declare no competing interests.

References

1. Fu MW, Wang JL (2021) Size effects in multi-scale materials processing and manufacturing. Int J Mech Tools Manuf 167:103755
2. Chan WL, Fu MW, Lu J, Liu JG (2010) Modeling of grain size effect on micro deformation behavior in micro-forming of pure copper. Mater Sci Eng A 527:6638–6648
3. Qu FJ, Jiang ZY, Wei DB, Chen QQ, Lu HN (2017) Study of micro flexible rolling based on grained inhomogeneity. Int J Mech Sci 123:324–339
4. Shimizu T, Ogawa M, Yang M, Manabe K (2014) Plastic anisotropy of ultra-thin rolled phosphor bronze foils and its thickness strain evolution in micro-deep drawing. Mater Des 56:604–612
5. Wang S, Chen ZH, Dong CF (2017) Tearing failure of ultra-thin sheet metal involving size effect in blanking process: analysis based on modified GTN model. Int J Mech Sci 133:288–302
6. Veenaas S, Vollertsen F (2014) High speed joining by laser shock forming. Adv Mat Res 966–967:597–606
7. Veenaas S, Wielage H, Vollertsen F (2014) Joining by laser shock forming: realization and acting pressures. Prod Eng 8:283–290
8. Ji Z, Liu R, Wang DG, Zhang MH, Su QC (2008) A micro clinching method and its device for joining ultra-thin sheets with pulsed laser. Chinese Patent
9. Veenaas S, Vollertsen F (2018) Mechanical joining of glass and aluminium. Key Eng Mater 767:369–376
10. Veenaas S, Vollertsen F, Czotscher T (2019) Joining by laser induced shock waves of aluminum and plastics. AIP Confer Proc 2113:050029
11. Wang XY, Ji Z, Wang JF, You SX, Zheng C, Liu R (2018) An experimental and numerical study on laser shock clinching for joining copper foil and perforated stainless steel sheet. J Mater Process Technol 258:155–164
12. Wang XY, Ji Z, Zheng C, Liu R (2020) Joining similar and dissimilar material combinations by laser shock forming. J Manuf Process 60:318–327
13. Zheng C, Zhang Y, Zhao G, Ji Z, Sun Y (2020) Influence of process parameters on forming quality of Cu–Fe joints by laser shock hole-clinching. Int J Adv Manuf Technol 110:887–898
14. Hou YX, Ding KX, Lu GX, Zheng C, Ji Z (2022) Investigation of microscale laser shock flat hole clinching. Int J Precis Eng Manuf 23:1019–1025
15. Zheng C, Zhang X, Liu Z, Ji Z, Yu X, Song LB (2018) Investigation on initial grain size and laser power density effects in laser shock bulging of copper foil. Int J Adv Manuf Technol 96:1483–1496
16. Li HY, Yu S, Li JH (2020) Crystal plasticity finite element simulation of aluminium deformation. Mater Sci Forum 1001:127–132
17. Zhang HM, Dong XH (2015) Physically based crystal plasticity FEM including geometrically necessary dislocations: numerical implementation and applications in micro-forming. Comput Mater Sci 110:308–320
18. Barrett TJ, Knezevic M (2019) Deep drawing simulations using the finite element method embedding a multi-level crystal plasticity constitutive law: experimental verification and sensitivity analysis. Comput Methods Appl Mech Eng 354:245–270
19. Kardan-Halvaei M, Morovvati MR, Mollaei-Dariani B (2020) Crystal plasticity finite element simulation and experimental investigation of the micro-upsetting process of OFHC copper. J Micromech Microeng 30:075005
20. Xu ZF, Zhang CS, Wang KZ, Zhang K, Zhao GQ, Chen L (2020) Crystal plasticity prediction of texture evolution during helical extrusion process of aluminium alloys under three-dimensional deformation path. J Alloys Compd 830:154598

21. Tang XF, Peng LF, Shi SQ, Fu MW (2019) Influence of crystal structure on size dependent deformation behavior and strain heterogeneity in micro-scale deformation. Int J Plast 118:147–172
22. Zhao M, Mao J, Ji X, Feng YX, Liang SY (2021) Effect of crystallographic orientation on residual stress induced in micro-grinding. Int J Adv Manuf Technol 112:1271–1284
23. Wang C, Wu H, Wang XG, Wang CL, Wang L (2020) Numerical study of microscale laser bulging based on crystal plasticity. Int J Mech Sci 177:105553
24. Fabbro R, Fournier J, Ballard P, Devaux D, Virmont J (1990) Physical study of laser-produced plasma in confined geometry. J Appl Phys 68:775–784
25. Peyre P, Fabbro R, Merrien P, Lieurade HP (1996) Laser shock processing of aluminium alloys. Application to high cycle fatigue behaviour. Mater Sci Eng A 210:102–113
26. Wang J, Wang YQ, Wang S, Lu GX, Zheng C, Ji Z (2021) Experimental and FEM investigation on incremental laser shock clinching for joining three sheets of copper/aluminum/stainless steel. Optics Laser Technol 141:107141
27. Zhang WW, Yao YL (2002) Micro scale laser shock processing of metallic components. J Manuf Sci Eng 124:369–378
28. Asaro RJ, Rice JR (1997) Strain localization in ductile single crystals. J Mech Physic Solids 25:309–338
29. Peirce D, Asaro RJ, Needleman A (1983) Material rate dependence and localized deformation in crystalline solids. Acta Metall 31:1951–1976
30. Anand L, Kothari M (1996) A computational procedure for rate-independent crystal plasticity. J Mech Physic Solids 44:525–558
31. Shahba A, Ghosh S (2016) Crystal plasticity FE modeling of Ti alloys for a range of strain-rates. Part I: a unified constitutive model and flow rule. Int J Plast 87:48–68
32. Luscher DJ, Bronkhorst CA, Alleman CN, Addessio FL (2013) A model for finite-deformation nonlinear thermomechanical response of single crystal copper under shock conditions. J Mech Phys Solids 61:1877–1894
33. Wang C, Wang XG, Wang CL, Wu G, Lai YB (2021) A comparative study of plastic deformation behaviors of OFHC copper based on crystal plasticity models in conjunction with phenomenological and dislocation density-based hardening laws. J Mater Sci 56:8789–8814
34. Houtte PV, Kanjarla AK, Bael AV, Seefeldt M, Delannay L (2006) Multiscale modelling of the plastic anisotropy and deformation texture of polycrystalline materials. Eur J Mech A/Solids 25:634–648
35. Kalidindi SR, Bronkhorst CA, Anand L (1992) Crystallographic texture evolution in bulk deformation processing of FCC metals. J Mech Phys Solids 40:537–569